Journal of Advanced Ceramics
2022, **11**(7): 1069–1081
https://doi.org/10.1007/s40145-022-0590-6
ISSN 2226-4108
CN 10-1154/TQ

Research Article

Coupling of piezocatalysis and photocatalysis for efficient degradation of methylene blue by $Bi_{0.9}Gd_{0.07}La_{0.03}FeO_3$ nanotubes

Angom Devadatta MANI[a,b,†], Jie LI[a,b,†], Ziquan WANG[c], Jiale ZHOU[a], Huaicheng XIANG[a], Jinlai ZHAO[a], Libo DENG[c], Haitao YANG[a], Lei YAO[a,*]

[a]*Shenzhen Key Laboratory of Special Functional Materials*, *Shenzhen Engineering Laboratory for Advanced Technology of Ceramics*, *Guangdong Research Center for Interfacial Engineering of Functional Materials*, *College of Materials Science and Engineering*, *Shenzhen University*, *Shenzhen 518071*, *China*
[b]*Key Laboratory of Optoelectronic Devices and Systems of Ministry of Education and Guangdong Province*, *College of Optoelectronic Engineering*, *Shenzhen University*, *Shenzhen 518060*, *China*
[c]*College of Chemistry and Environmental Engineering*, *Shenzhen University*, *Shenzhen 518071*, *China*

Received: January 12, 2022; Revised: March 14, 2022; Accepted: March 23, 2022

Abstract: Photocatalytic degradation of organic pollutants is of great significance for wastewater remediation but is still hindered by the poor catalytic efficiency of the catalysts. Herein, we report a strategy to simultaneously introduce piezocatalysis and to enhance the intrinsic photocatalysis in a single catalyst, which improved the performance for catalytic degradation of methylene blue (MB) significantly. Specifically, piezoelectric $BiFeO_3$ (BFO) nanotube doped with different contents of Gd and La ($Bi_{0.9}(Gd_xLa_{1-x})_{0.1}FeO_3$) were produced by electrospinning. The doping led to a higher concentration of surface oxygen vacancy (OV) in $Bi_{0.9}Gd_{0.07}La_{0.03}FeO_3$, which effectively increased the piezoelectric field due to the deformation of BFO, and suppressed the recombination of photon-generated electron–hole pairs. The $Bi_{0.9}Gd_{0.07}La_{0.03}FeO_3$ nanotube showed excellent catalytic performance under simultaneous light irradiation and ultrasonic excitation, giving an extraordinary 95% degradation of MB within 90 min. These findings suggest that the piezoelectric effect combined with defect engineering can enhance the catalytic performance of $Bi_{0.9}Gd_{0.07}La_{0.03}FeO_3$ nanotube. This could potentially be extended to other catalytic systems for high-performance pollutant treatment.

Keywords: photocatalysis; piezocatalysis; sonophotocatalysis; oxygen vacancy (OV)

1 Introduction

The remediation of wastewater containing high concentrations of organic dyes discharged by textiles, tanning, and other industries has attracted substantial attention due to their threat to human health [1,2]. Energy limitations necessitate harvesting and utilizing various forms of sustainable energy for water purification. Photocatalysis is an oxidation technology which has been regarded as a breakthrough in harvesting solar energy to realize dye decomposition [3]. The relatively low photocatalytic activity under visible light and the

† Angom Devadatta Mani and Jie Li contributed equally to this work.

* Corresponding author.
E-mail: lyao@szu.edu.cn

fast recombination of photo-generated electron–hole pairs currently limit the solar-light-driven photocatalytic efficiency. Strategies including band gap engineering, heterostructure modulating, and noble metal decorating have been developed to lower the recombination rate and increase the lifetime of photo-generated charge carriers [4–9]. While much progress has been made, further effort is required to satisfactorily enhance the visible-light-driven photocatalytic activity.

In photocatalysis, photo-induced electric charges (electron–hole pairs) participate in catalytic redox reactions. Piezoelectric charges (positive and negative charges) induced by mechanical vibrations can also be used to drive catalytic redox reactions, which is known as piezocatalysis [10–12]. Moreover, an internal electric field is generated during the vibration energy harvesting process of piezoelectric materials which can further promote charge carrier separation [13,14]. Piezoelectric nanomaterials including $BaTiO_3$, MoS_2, ZnO, BiOCl, and $KNbO_3$ have demonstrated great potential in environmental remediation because of their piezocatalytic effects that can be induced by weak mechanical forces [11,14–19]. This could increase the application of green technologies by harnessing renewable solar energy and utilization of the underexploited mechanical energy such as noise and vibrations for environmental remediation. However, there is still space to develop more efficient piezoelectric catalysts to enhance the photocatalysis efficiency.

Another effective strategy to enhance the photocatalysis performance is through modulating the surface oxygen vacancies (OVs) [20]. OVs act as electron trapping centers near the bottom of the conduction band (CB) and prevent the recombination of photo-generated charge carriers. This facilitates the holes in the valence band (VB) to undergo oxidation, thus enhancing the photocatalytic activity [21–24]. OVs also play a role in reducing the energy band gap (E_g) and extending the light absorption into the visible/infrared region [25]. Oxygen defective-enhancement may therefore offer opportunities to engineer and improve the performance of piezoelectric photocatalysis. $BiFeO_3$ (BFO) is a piezoelectric material with photocatalytic activity under visible light. The narrow band gap of BFO permits a broad absorption of visible wavelengths up to 750 nm [26]. It has been demonstrated that the piezoelectric properties of BFO are extremely sensitive to defects, particularly OVs [27,28]. Therefore, combining piezo-photocatalysis with defective OV engineering to couple the electron trapping effect and piezoelectric effect in BFO may further increase its piezo/photocatalytic activity. Particularly, doping of BFO by certain isovalent cations is an effective way to introduce defective OVs and to enhance photocatalytic efficiency [29,30]. Previous studies have reported that Gd-doped BFO can enhance visible light photocatalytic activity in the photodegradation of organic dyes [31], and La-doped magnetic BFO-based multiferroics can degrade 94.5% of carbamazepine by piezocatalysis in 30 min for water purification [32]. Piezoelectric BFO also showed great promise for boosting hydrogen evolution [33]. Also, due to the smaller ionic radii of La^{3+} compared to Bi^{3+}, doping La into BFO can increase magnetization. Moreover, the La dopant in the BFO can improve the separation and migration of photo-generated charge carriers and decrease the electron–hole pair recombination probability [34].

In this work, we developed a facile method to simultaneously introduce piezocatalysis and to enhance the intrinsic photocatalysis in a single catalyst. BFO nanotubes doped with different contents of Gd and La were fabricated through electrospinning. The concentration of OVs in $Bi_{0.9}(Gd_xLa_{1-x})_{0.1}FeO_3$ (x = 0, 0.3, 0.5, 0.7, and 1.0) was optimized by changing the ratios of Gd and La dopants. Stimuli by both light and mechanical strain (ultrasonication) were used to study the piezo-/photo-catalytic degradation of model organic pollutant methylene blue (MB). The defect-induced OVs in $Bi_{0.9}Gd_{0.07}La_{0.03}FeO_3$ could enhance the intrinsic photocatalytic performance, while combined with the piezoelectric-enhanced charge separation and improved the overall performance. Specifically, $Bi_{0.9}Gd_{0.07}La_{0.03}FeO_3$ showed an extraordinary MB degradation efficiency of 95% within 90 min under simultaneous all-spectrum solar irradiation and ultrasonic excitation. The proposed defect engineering strategy provides a simple and low-cost way to prepare high-performance piezo-/photo-catalysts, which has a great potential in pollution remediation.

2 Experimental

2. 1 Preparation of the BFO-containing nanotubes

All chemical reagents were produced as analytical grade and used directly without any further purification. Pristine BFO and the doped BFO nanotubes with the compositional formula $Bi_{0.9}(Gd_xLa_{1-x})_{0.1}FeO_3$ (x = 0, 0.3, 0.5, 0.7, and 1.0) were prepared by a simple

electrospinning method. The precursor solution was prepared by a two-pot method. First, stoichiometric amount of bismuth nitrate pentahydrate ($Bi(NO_3)_3{\cdot}5H_2O$, Mreda, USA), iron nitrate nonahydrate ($Fe(NO_3)_3{\cdot}9H_2O$, Macklin, China), gadolinium nitrate hexahydrate ($Gd(NO_3)_3{\cdot}6H_2O$, Macklin, China), and lanthanum nitrate hexahydrate ($La(NO_3)_3{\cdot}6H_2O$, Macklin, China) were dissolved in 2-methoxyethanol (Damas-beta, China) with the molarity of 0.2 M. Subsequently, citric acid monohydrate (Damas-beta, China) was added as the chelating agent to expedite the binding process of the metal ions. Finally, 3 M HNO_3 acid was added to remove the impurities in the solution. 1 g polyvinyl pyrrolidone (PVP, Macklin, China) (M_w = 1,300,000) was added to 10 mL dimethyl formamide (DMF, Macklin, China) to obtain a viscous solution. Both these solutions were mixed and stirred continuously for 8 h at room temperature to obtain a homogeneous solution for the electrospinning process. The obtained solution was then fed into a 20 mL plastic syringe, and a high voltage of 15 kV was applied to the stainless steel needle. The flow rate of the solution was maintained at 0.3 $mL{\cdot}h^{-1}$, and the as-spun nanofibers were collected on an aluminum spread roller of 100 mm in diameter, rotating at a speed of 250 $r{\cdot}min^{-1}$. The distance between the needle tip and the roller was fixed at 15 cm. The as-collected nanofibers were dried in an oven at 200 ℃ for 2 h, followed by calcination at 550 ℃ for 30 min in air atmosphere.

2. 2 Material characterization

The crystal structures of the samples were characterized by the X-ray diffractometer (Bruker AXS, WI, USA) using Cu Kα radiation (λ = 1.5418 Å). The refined lattice parameters were obtained from the Rietveld refinement of the X-ray diffraction (XRD) data using Fullprof software. Structural deformation and lattice shifting in the host lattice were determined by the Raman spectroscope (Invia Reflex, Renishaw). The surface morphology and the quantitative elemental content were characterized by the field emission scanning electron microscope (FESEM; SU-70, Hitachi, Japan) attached with an energy dispersive X-ray spectroscope (EDS; Oxford INCA, UK). The microstructure of the nanotube was also inspected by the transmission electron microscope (TEM; JEM-2100, JEOL, Japan). The elemental composition and chemical binding states of the various ions presented in the synthesized samples were analyzed by the X-ray photoelectron spectroscope (XPS; Thermo Fisher Scientic ESCALAB 250Xi, USA). The optical absorption spectra of all the samples were recorded on an ultraviolet–visible spectrophotometer (Lambda 950, Perkin Elmer, USA) in the wavelength range of 200–800 nm, and the E_g values were obtained from Tauc plot. The rate of the recombination of the photo-generated electron and hole was characterized by the photoluminescence (PL; Edinburgh FS5, Edinburgh Instruments, UK) equipped with a Xenon lamp at an excitation wavelength of 400 nm. The piezoresponse force microscope (PFM; Bruker, Billerica, MA, USA) was performed to characterize the piezoelectric properties of the synthesized samples.

2. 3 Dye degradation measurements

Different catalytic experiments were performed to investigate the degradation of MB by using the synthesized samples as the catalysts. The concentration of the MB solution was maintained at 20 $mg{\cdot}L^{-1}$ for all the experiments, and 45 mg of the calcined nanotubes were dispersed in 100 mL of MB solution under continuous stirring. The solution mixture was stirred continuously for 1 h to reach the adsorption–desorption equilibrium before starting the experiments. The temperature was maintained at 20 ℃ by adding ice bags during the whole reaction to eliminate the influence of thermal heating on the experiments. For the piezocatalytic (sonocatalytic) tests, the samples were exposed to mechanical vibrations by using an ultrasonic source supplied by a sonicator (120 W, 40 kHz). The whole setup was placed in a dark environment to avoid the degradation by light exposure. For the photocatalytic tests, the samples were irradiated with an ultraviolet–visible (UV–Vis) light using a 300 W Xenon lamp equipped with an air mass (AM) 1.5G solar simulator as the source. For the piezophotocatalytic (sonophotocatalytic) tests, both the above-mentioned ultrasonic and light sources were used simultaneously. Then, 4 mL of the solution mixture was collected after each 15 min and centrifuged at 12,000 $r{\cdot}min^{-1}$ for 10 min to remove the catalyst powders. The concentration of the resulting MB solution was then measured at the maximum absorbance at 664 nm using a UV–Vis spectrophotometer. For the stability test, the remaining powders after the experiment were collected by centrifugation, washed with deionized (DI) water several times to remove the residual MB, and dried for the next test cycle. The test was repeated for ten times to check the reproducibility.

2. 4 Photoelectrochemical measurements

An electrochemical system (CHI760E, CH instruments, China) was used to measure the photocurrent response during an on–off state of the light exposure on a three-electrode system using a 0.5 M Na_2SO_4 electrolyte. The working electrode with an exposure area of 1 cm × 1 cm was prepared by loading the slurry mixture, which consists of the nanotubes and Nafion binder, onto the surface of Ni foam and followed by drying at 60 ℃ for 12 h. A Pt wire was used as the counter electrode, and a standard Ag/AgCl was used as the reference electrode. The photocurrent response was recorded by a periodic on-off reversal of light after each 100 s.

3 Results and discussion

3. 1 Structural characterization

Electrospinning is a powerful technique to fabricate one-dimensional nanostructures (typically nanofibers). All the electrospun BFO and $Bi_{0.9}(Gd_xLa_{1-x})_{0.1}FeO_3$ (x = 0, 0.3, 0.5, 0.7, and 1.0) exhibit hollow fibrous morphology, as seen from the FESEM images shown in Fig. S1 in the Electronic Supplementary Material (ESM). Specifically, $Bi_{0.9}Gd_{0.07}La_{0.03}FeO_3$ exhibits a nanotube structure with an average diameter of ~71 nm (Figs. 1(a)–1(c)). The TEM image shows that the thickness of the nanotube wall is ~100 nm (Fig. 1(d)), and the average grain size is ~10 nm (Fig. 1(e)). The interplanar distances of 0.28 and 0.39 nm correspond to the (104) and (012) planes of the perovskite phase of BFO, respectively, and are in good agreement with the selected area electron diffraction (SAED) pattern (the inset in Fig. 1(e)) [35,36]. EDS mapping images indicate uniform distributions of Bi, Gd, La, and Fe in the $Bi_{0.9}Gd_{0.07}La_{0.03}FeO_3$ nanotubes (Fig. S2 in the ESM). The formation of the tubular morphology is attributed to the Kirkendall effect (Fig. 1(f)) [37,38]. During the Kirkendall oxidation, metal (M) ions diffuse outwards whereas oxygen (O) ions diffuse inwards, forming a continuous layer of metal–oxygen (M–O) bonds near the interface. This layer remains an oxygen-deficient state because of the slower diffusion of O compared to M. This unbalanced diffusion results in the diffusion of vacancies, which leads to the formation of Kirkendall holes (H) near the interface in the side with the higher diffusion rate [37,39]. The tubular morphology, small grain size, and small diameter of the doped BFO nanotubes give rise to a high surface area potentially available for catalytic activity.

Figure 2(a) shows the XRD patterns of BFO and $Bi_{0.9}(Gd_xLa_{1-x})_{0.1}FeO_3$ (x = 0, 0.3, 0.5, 0.7, and 1.0). All peaks can be indexed to the rhombohedrally-distorted

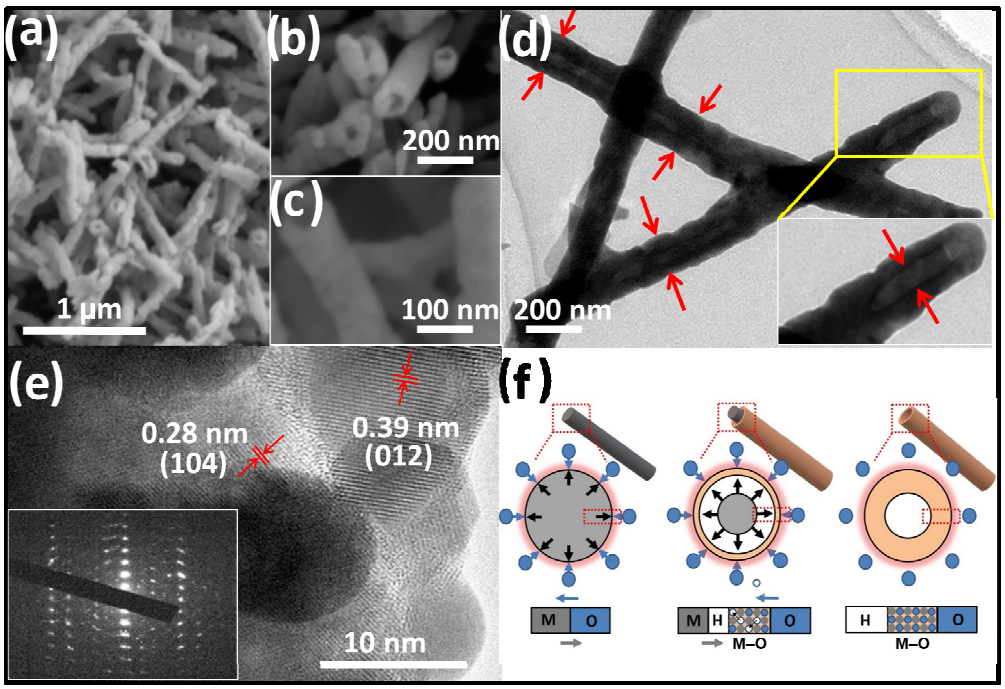

Fig. 1 Morphologies of $Bi_{0.9}Gd_{0.07}La_{0.03}FeO_3$ nanotubes: (a–c) FESEM images, (d) TEM image, (e) HRTEM image with the SAED pattern inset, and (f) schematic illustration of the formation mechanism of the tubular nanostructure.

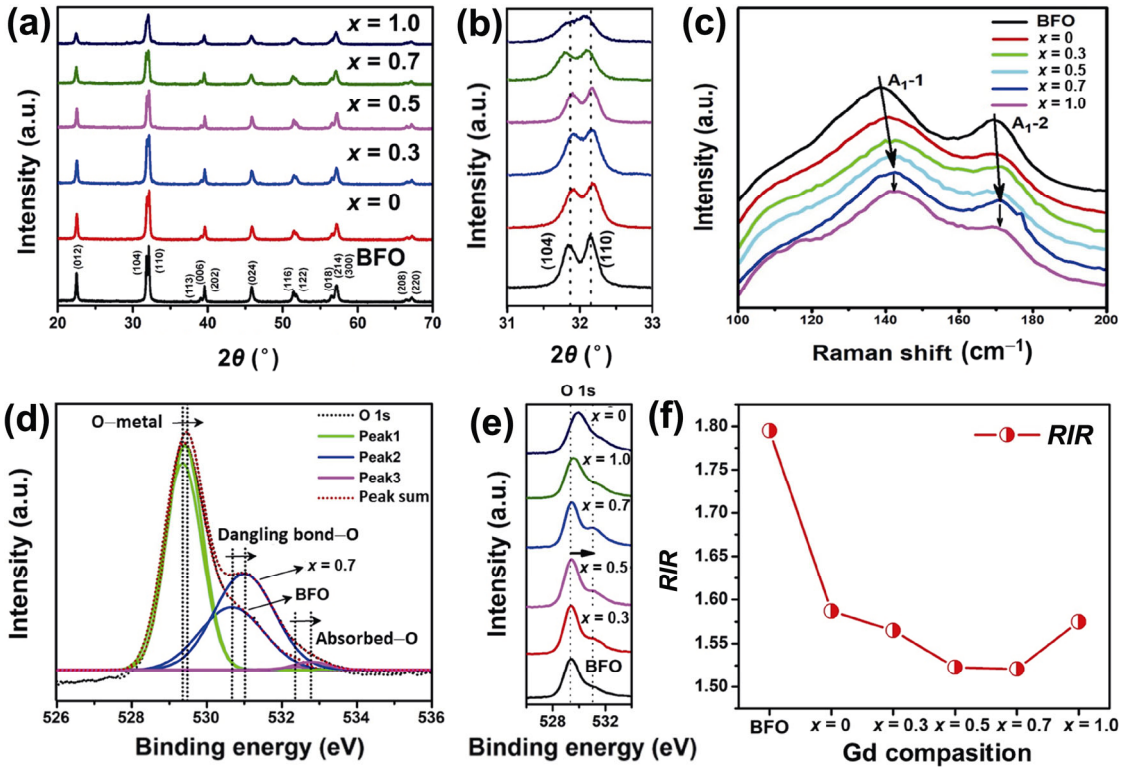

Fig. 2 Crystal structures and chemical structures of BFO and $Bi_{0.9}(Gd_xLa_{1-x})_{0.1}FeO_3$ (x = 0, 0.3, 0.5, 0.7, and 1.0): (a) XRD patterns, (b) magnified XRD patterns in the range of 31°–33°, (c) Raman spectra, (d) O 1s XPS spectra of $Bi_{0.9}Gd_{0.07}La_{0.03}FeO_3$, (e) O 1s XPS spectra of all the samples, and (f) relationship between the relative peak intensity ratio (*RIR*) and the content of Gd.

perovskite BFO phase with *R*3*c* space group without any impurities. This indicates the good dispersion of Gd^{3+} and La^{3+} in the BFO lattice [27,28]. Increasing the Gd^{3+} content leads to gradual broadening in the (104) and (110) peaks which eventually merge into a single peak at a lower diffraction angle (Fig. 2(b)). The crystallite size and lattice constant decrease with the increase of Gd^{3+} content (Table S1 in the ESM). This reveals the evolution of lattice deformation in the crystal structure due to the A-site substitution [40,41]. Compared to the La-rich samples ($x < 0.5$), the Gd-rich samples ($x > 0.5$) have smaller crystallite sizes and larger deformation in the crystal lattice. This is attributed to the larger difference in the ionic radii of Gd^{3+} (0.94 Å) and Bi^{3+} (1.03 Å) compared with those of La^{3+} (1.06 Å) and Bi^{3+} (1.03 Å) at the A-site [36].

The Raman spectroscopy was used to investigate lattice disorder and the associated defect formation upon introducing dopants. Eleven fundamental modes are observed in the Raman spectra of BFO and $Bi_{0.9}(Gd_xLa_{1-x})_{0.1}FeO_3$ (x = 0, 0.3, 0.5, 0.7, and 1.0) in the range of 100–800 cm^{-1} (Fig. S3 in the ESM). All these vibrational phonon modes suggest a rhombohedral structure and are in agreement with the reported values [42,43]. Peaks at 137, 169, 217, and 471 cm^{-1} are the A_1 modes, and peaks at 261, 276, 306, 346, 369, 526, and 597 cm^{-1} are the E modes of BFO. A_1 and E modes at wavenumbers smaller than 400 cm^{-1} correspond to the Bi–O bond, whereas peaks at wavenumbers above 400 cm^{-1} correspond to the Fe–O bond [42]. Increasing the Gd ratio from 0 to 0.7 leads to the peaks of the A_1-1 and A_1-2 modes gradually broadening and shifting towards higher wavenumbers (Fig. 2(c)). This suggests that the substitution of Gd^{3+} and La^{3+} at the Bi-site changes the vibration motion in the FeO_6 octahedra. The Raman shift and peak broadening can be attributed to the reduction of particle size and formation of OVs upon doping [44].

The surface compositions and valence states were further analyzed using XPS. Figure S4 in the ESM shows the XPS spectra of the Bi 4f, Fe 2p, Gd 4d, and La 3d regions for all the samples. The deconvolution of the Bi ($4f_{7/2}$ and $4f_{5/2}$), Fe ($2p_{3/2}$ and $2p_{1/2}$), Gd ($4d_{5/2}$ and $4d_{3/2}$), and La ($3d_{5/2}$ and $3d_{3/2}$) peaks suggests +3 oxidation states for these four elements. The O 1s spectrum of $Bi_{0.9}Gd_{0.07}La_{0.03}FeO_3$ can be resolved into three peaks at 529.4, 531.0, and 532.8 eV, which are attributed to the O–M bond, dangling bond-O, and

absorbed-O, respectively (Fig. 2(d)) [45]. The emergence of dangling bond-O and adsorbed-O has been suggested to be related to the formation of OVs in the host lattice of perovskite oxides [41]. The concentration of OVs can be approximately estimated by *RIR* given by Eq. (1):

$$RIR = \frac{I_{O-M}}{I_{DL} + I_{ADS}} \quad (1)$$

where I_{O-M} is the relative peak intensity of the O–M bond, I_{DL} is the relative peak intensity of the dangling bond, and I_{ADS} is the relative peak intensity of adsorbed oxygen [46]. A smaller *RIR* value indicates a higher concentration of OVs [47]. The *RIR* values of the pristine BFO and $Bi_{0.9}(Gd_xLa_{1-x})_{0.1}FeO_3$ (x = 0, 0.3, 0.5, 0.7, and 1.0) are calculated according to the peak intensities of the samples in Fig. 2(e) and are displayed in Fig. 2(f). The *RIR* decreases with the increase of Gd content, reaching a minimum value at around x = 0.7. This indicates that OVs are introduced into the BFO crystal lattice due to the Gd and La doping, and the $Bi_{0.9}Gd_{0.07}La_{0.03}FeO_3$ nanostructure has the most abundant OVs.

3. 2 Optical and piezoelectric properties

Figure 3(a) shows the room-temperature UV–Vis absorption spectra of BFO and $Bi_{0.9}(Gd_xLa_{1-x})_{0.1}FeO_3$ (x = 0, 0.3, 0.5, 0.7, and 1.0) nanotubes. Upon doping, the absorption spectra shift from the UV region to the visible region. The optical absorption coefficient ($\alpha h\nu$) follows the Tauc relationship described by Eq. (2):

$$(\alpha h\nu)^n = A(h\nu - E_g) \quad (2)$$

where A, α, h, and ν are a constant, absorption coefficient, Planck's constant, and frequency of incident photons, respectively. The corresponding E_g can be estimated from the Kubelka–Munk (K–M) theory by extrapolating the linear portion of the $(\alpha h\nu)^n$ vs. $h\nu$ plot to the $h\nu$ axis (in which the value for n was 2 for calculating indirect bandgap) [35]. The good linear fit above the band gap indicates the direct band gap behavior of the nanotubes (Fig. S5 in the ESM) [48]. The calculated E_g values are 2.9, 2.7, 2.5, 2.3, 2.1, and 2.4 eV for BFO and $Bi_{0.9}(Gd_xLa_{1-x})_{0.1}FeO_3$ (x = 0, 0.3, 0.5, 0.7, and 1.0), respectively, which are shown in Fig. 3(b). The trend of variation in E_g coincides with that in the *RIR* values of the doped BFO nanotubes, revealing a strong relationship between the decrease of E_g and the introduction of OVs. In the pristine BFO, E_g is the region between the O 2p and Fe 3d hybrid states. Introducing OVs creates new sub-band defect states by lowering the adjacent 3d levels, which decreases the overall E_g [49]. The $Bi_{0.9}Gd_{0.07}La_{0.03}FeO_3$ nanotube shows the largest shift and smallest E_g due to the highest concentration of OVs, which indicates that it can absorb and utilize more visible light from the solar spectrum than the other samples.

To elucidate the effect of Gd and La doping and the introduction of OVs on the charge carrier excitation/separation ability of the nanotubes, PL spectra of BFO and $Bi_{0.9}(Gd_xLa_{1-x})_{0.1}FeO_3$ (x = 0, 0.3, 0.5, 0.7, and 1.0) were recorded using an excitation wavelength of 400 nm (Fig. 3(c)). All the PL spectra show two visible light emissions, i.e., blue emission (BE) at 491.0 nm (2.52 eV) and yellow emission (YE) at 580.8 nm (2.13 eV). The BE corresponds to the near band emission (NBE) which is characteristic of the radiative transition of photo-generated charge carriers [48]. A stronger PL peak usually implies a higher chance of recombination between electrons and holes. When the Gd doping ratio increases from 0 to 0.7, the peak intensity of the NBE peak gradually decreases, indicating that the $Bi_{0.9}Gd_{0.07}La_{0.03}FeO_3$ nanotube has the lowest radiative recombination rate [41].

The time-dependent photocurrents of BFO and $Bi_{0.9}(Gd_xLa_{1-x})_{0.1}FeO_3$ (x = 0, 0.3, 0.5, 0.7, and 1.0) nanotubes were measured under solar irradiation (on–off interval of 100 s) to investigate the charge trapping and separation efficiency of the photo-generated charge carriers. A higher photocurrent response implies a higher charge carrier density and efficient charge carrier separation, which is beneficial to photocatalytic performance. As shown in Fig. 3(d), the doped BFO samples exhibit higher photocurrents than that of the pristine one, revealing a longer lifespan and more efficient separation of photo-generated charge carriers [41]. The current appeared and disappeared with reproducible curves in the presence of BFO and doped BFO samples, which indicates the separation and migration of electric charges in the flowing system [50]. This is consistent with the PL spectra and the photocatalytic performance results (discussed below). The $Bi_{0.9}Gd_{0.07}La_{0.03}FeO_3$ nanotube exhibits the highest photocurrent intensity which indicates the highest photoconversion ability and charge separation, and thus it is expected to exhibit the highest photocatalytic activity. It is known that the chemisorption of gas molecules such as O_2 and H_2O occurs at the surface and depletes the free electrons in the nanotube, i.e.,

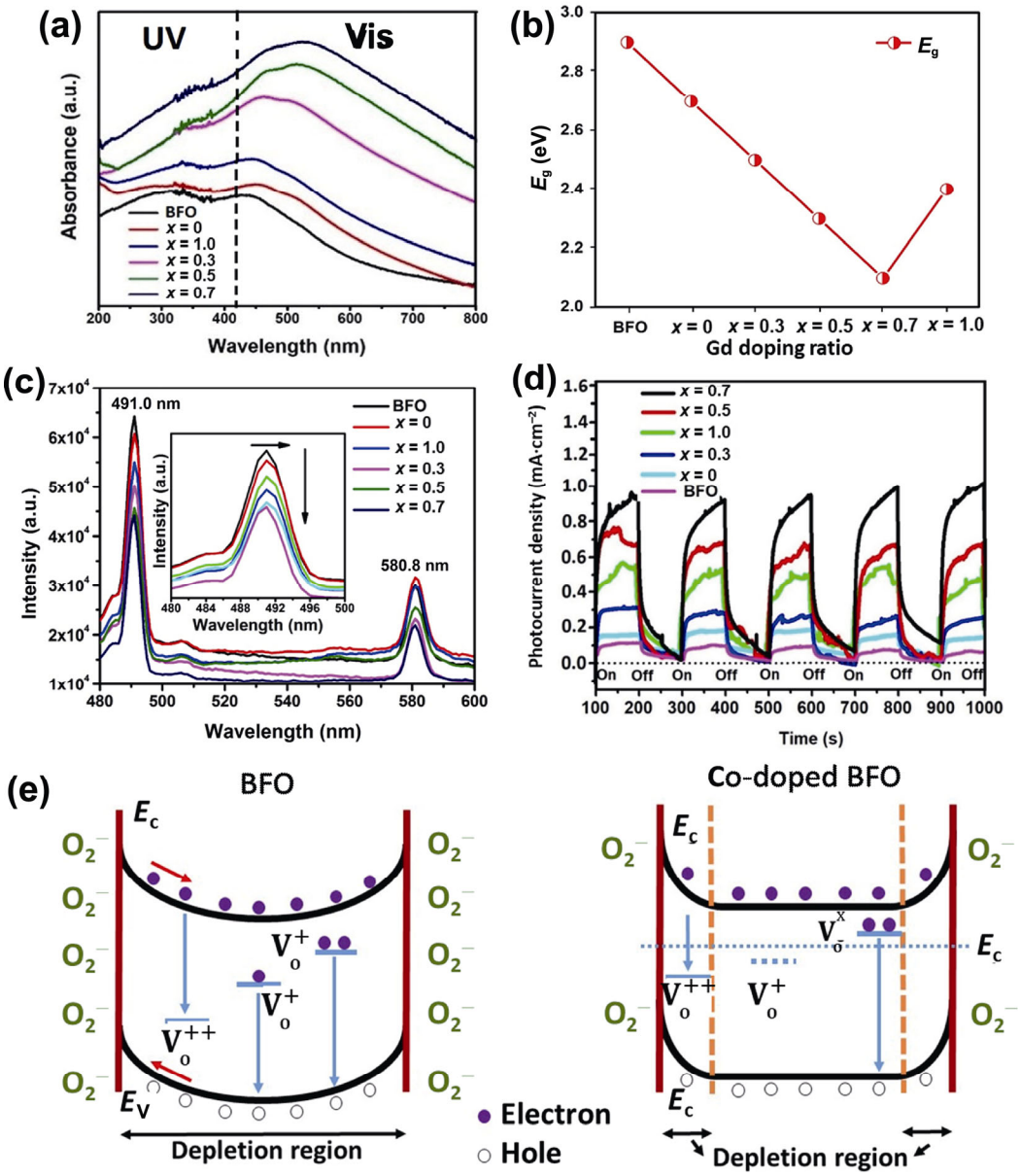

Fig. 3 Effect of introduced OVs in BFO on the band structure and optical properties: (a) UV–Vis absorbance spectra in the wavelength range of 200–800 nm, (b) relationship between E_g and Gd doping ratio, (c) PL spectra with the magnified spectra inset, (d) transient photocurrent response with light on/off cycles of 100 s, and (e) schematic illustration of the charge trapping mode of OVs in BFO and co-doped BFO nanotubes.

$O_2 + e^- \rightarrow O_2^-$ and $2H_2O + O_2 + 4e^- \rightarrow 4OH^-$ [51]. OVs at the surface act as adsorption sites to donate free electrons, resulting in three charge states, i.e., doubly ionized oxygen vacancies (V_O^{++}) (no electron captured), singly ionized oxygen vacancies (V_O^+) (one electron captured), and neutral oxygen vacancies (V_O^x) (two electrons captured) [52,53]. When the concentration of OVs is low, free electrons in the nanotubes are thoroughly depleted, and a wide depletion region and upward band bending form near the surface (as shown in the left panel of Fig. 3(e)). Doping the BFO nanotube with La and Gd increases the concentration of OVs, which decreases the thickness of the depletion layer at the surface (as shown in the right panel of Fig. 3(e)). The Fermi energy level would relocate to a higher energy level, preferably above the energy level of V_O^+ and V_O^{++} but below the energy level of V_O^x [52]. The narrow depletion layer at the surface tuned by OVs enables more holes to be captured by surface adsorbed oxygen ions, and fewer holes are left in the bulk to undergo radiative recombination with electrons [52]. The photo-generated electrons and holes segregate

in opposite directions across the depletion region near the surface, thereby reducing the recombination through excitonic processes. This potentially permits an enhanced photocatalytic efficiency because of the longer lifetime of the photo-generated charge carriers, which are then more likely to become active species such as OH· for subsequent MB degradation (schematically shown in Fig. 4, in which DB stands for dangling bond and E_f stands for the Fermi energy).

Piezoelectric properties of the samples were tested using the PFM. In the test, a conductive cantilever tip works in contact mode to provide an external bias on the sample, which is placed on a conductive substrate. Piezoelectric surface vibrations are induced in the sample. These vibrations are sensed through the cantilever deflection and the piezoresponse is measured [54–56]. Figures 5(a) and 5(e) show the phase contrast maps of the BFO and $Bi_{0.9}Gd_{0.07}La_{0.03}FeO_3$ nanotubes, and the corresponding amplitude maps are shown in Figs. 5(c) and 5(g). Regions with different phase contrasts, particularly the peripheries, represent domains with out-of-plane polarization alignments [57]. The amplitude images in Figs. 5(c) and 5(g) show that the ferroelectric domains are distributed randomly in different regions. The ferroelectric behavior of the pristine BFO and $Bi_{0.9}Gd_{0.07}La_{0.03}FeO_3$ nanotubes is confirmed by the piezoresponse phase–voltage hysteresis loops shown in Figs. 5(b) and 5(f) and the amplitude–voltage butterfly loops shown in Figs. 5(d) and 5(h). The phase loops show the polarization reversal of ferroelectricity when the tip bias is reversed. The amplitude–voltage loops show the characteristics of a butterfly loop, which is a strong indication of ferroelectricity rather than electrostatic interaction [56]. The distorted hysteresis of the butterfly loops may be attributed to several reasons including less tip bias voltage, inefficient electrical contact between the cantilever tip and sample, and the presence of a substantial amount of non-switchable components [58]. At −8 V, the amplitude for the $Bi_{0.9}Gd_{0.07}La_{0.03}FeO_3$ nanotube reaches 100 pm while that for the pristine BFO reaches 55 pm, which suggests the enhanced ferroelectric behavior of the $Bi_{0.9}Gd_{0.07}La_{0.03}FeO_3$ compared with the pristine BFO nanotube. The enhancement in ferroelectric properties is attributed to the induced lattice deformation due to A-site engineering by Gd and La dopants. The ferroelectric Bi^{3+}-sites (1.03 Å) are replaced by Gd^{3+} (0.94 Å) and La^{3+} ions (1.06 Å) with different sizes. Hence, a gradual lattice shifting is observed, ultimately changing the bond angles and bond length between the various ions. The off-centro symmetry of the BFO lattice is distorted. With the increase of Gd concentration, the amount of distortion of the symmetry increases, and hence the ferroelectric behavior increases [59]. The polarized ferroelectric domains could enhance the charge separation efficiency.

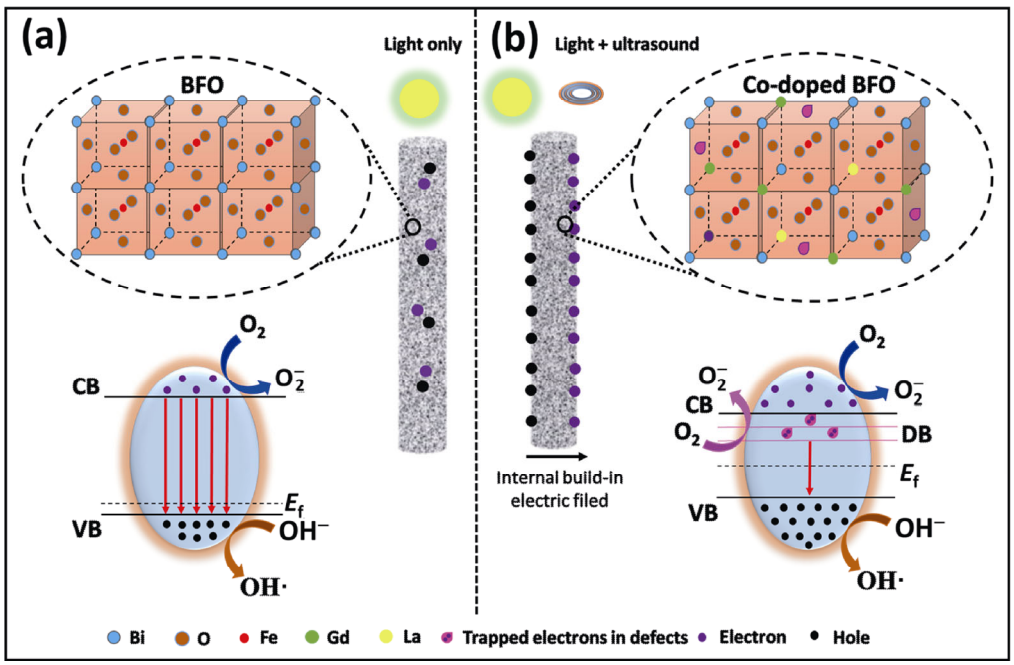

Fig. 4 Schematic illustration of the crystal structure and possible charge transfer mechanism: (a) BFO nanotubes under only light irradiation and (b) (Gd,La) co-doped BFO nanotubes under both light and ultrasound stimuli.

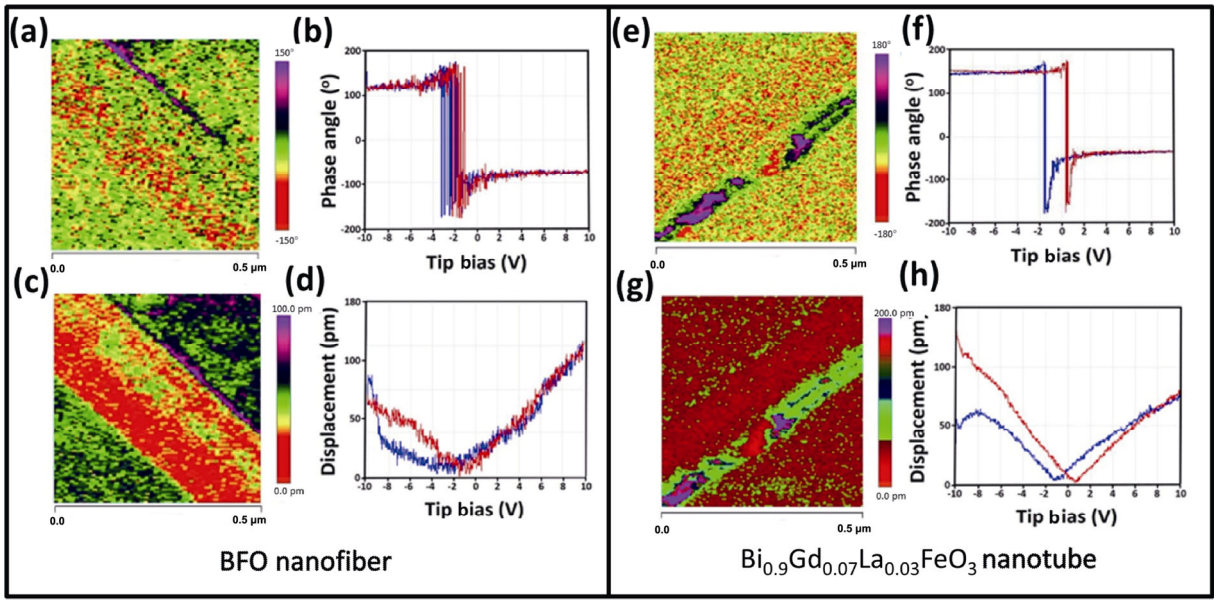

Fig. 5 PFM characterization of BFO and $Bi_{0.9}Gd_{0.07}La_{0.03}FeO_3$ nanotubes: (a, e) phase contrast maps; (b, f) phase–voltage hysteresis loops; (c, g) amplitude maps; and (d, h) amplitude–voltage butterfly loops.

3. 3 Performance for the catalytic degradation of MB

The degradation of MB under sonication excitation (sonocatalysis), solar irradiation (photocatalysis), and simultaneous sonication and solar irradiation (sono-photocatalysis) by BFO and $Bi_{0.9}(Gd_xLa_{1-x})_{0.1}FeO_3$ (x = 0, 0.3, 0.5, 0.7, and 1.0) nanotubes was investigated. The catalytic degradation efficiency can be monitored through the UV–Vis absorption spectrum of MB solution after irradiation and/or sonication excitation for different times in the presence of BFO or doped-BFO nanotubes (Figs. 6(a)–6(c) and Fig. S6 in the ESM). With the increase of exposure time, the intensity of the absorption peak at ~664 nm decreases, indicating the removal of MB dye from the solution. Figures 6(d)–6(f) show the C/C_0 ratio (where C and C_0 are the concentrations of MB at exposure time t and 0, respectively) of all the samples as a function of the exposure time. The MB degradation by the pristine BFO nanotube is ~7% under only vibration (i.e., under dark conditions). The vibration is introduced through the ultrasonic cavitation effect in the liquid solution at room temperature, which has been widely reported as an effective method to exert stress on nanomaterials [26]. The low MB sonocatalysis degradation of pristine BFO indicates that the polarization charges generated by the built-in electric field in BFO crystals under sonication are insufficient for the catalytic reaction to satisfactorily proceed. After doping with Gd and La, the MB degradation increases with the increase of Gd content and reaches a maximum of 37% for the $Bi_{0.9}Gd_{0.07}La_{0.03}FeO_3$ nanotube. This can be explained by the increase of the concentration of OVs upon doping which enhances the piezoelectric potential and electric charges generated via the piezoelectric effect as well as the active species to decompose MB [15,60].

Under solar irradiation, the degradation of MB in the presence of BFO nanotube is 71%, indicating a higher concentration of the photo-generated charge carriers than that in the case of sonocatalysis. In photocatalysis, O_2 is activated via the electrons excited in the CB or in localized states through photon absorption [61]. Upon doping, the concentration of OVs in the doped-BFO nanotube increases, and hence the affinity for O_2 to adsorb at the surface increases. These surface defects act as electron trapping centers localized below the CB, simultaneously reducing the band gap and increasing the lifetime of photo-generated charge carriers [52]. This increases the amount of photo-generated electrons and the active species such as $OH^{\cdot}$, and thus enhances the oxidation of MB (i.e., the intrinsic photocatalytic activity is enhanced). Among the doped catalysts, $Bi_{0.9}Gd_{0.07}La_{0.03}FeO_3$ has the highest concentration of OVs and the highest MB degradation of 89% within 90 min.

Under simultaneous sonication and solar irradiation, the MB degradation is further increased for all the BFO-containing nanotubes (Fig. 6(g)). For the pristine BFO nanotube, a MB degradation of 80% within 90 min

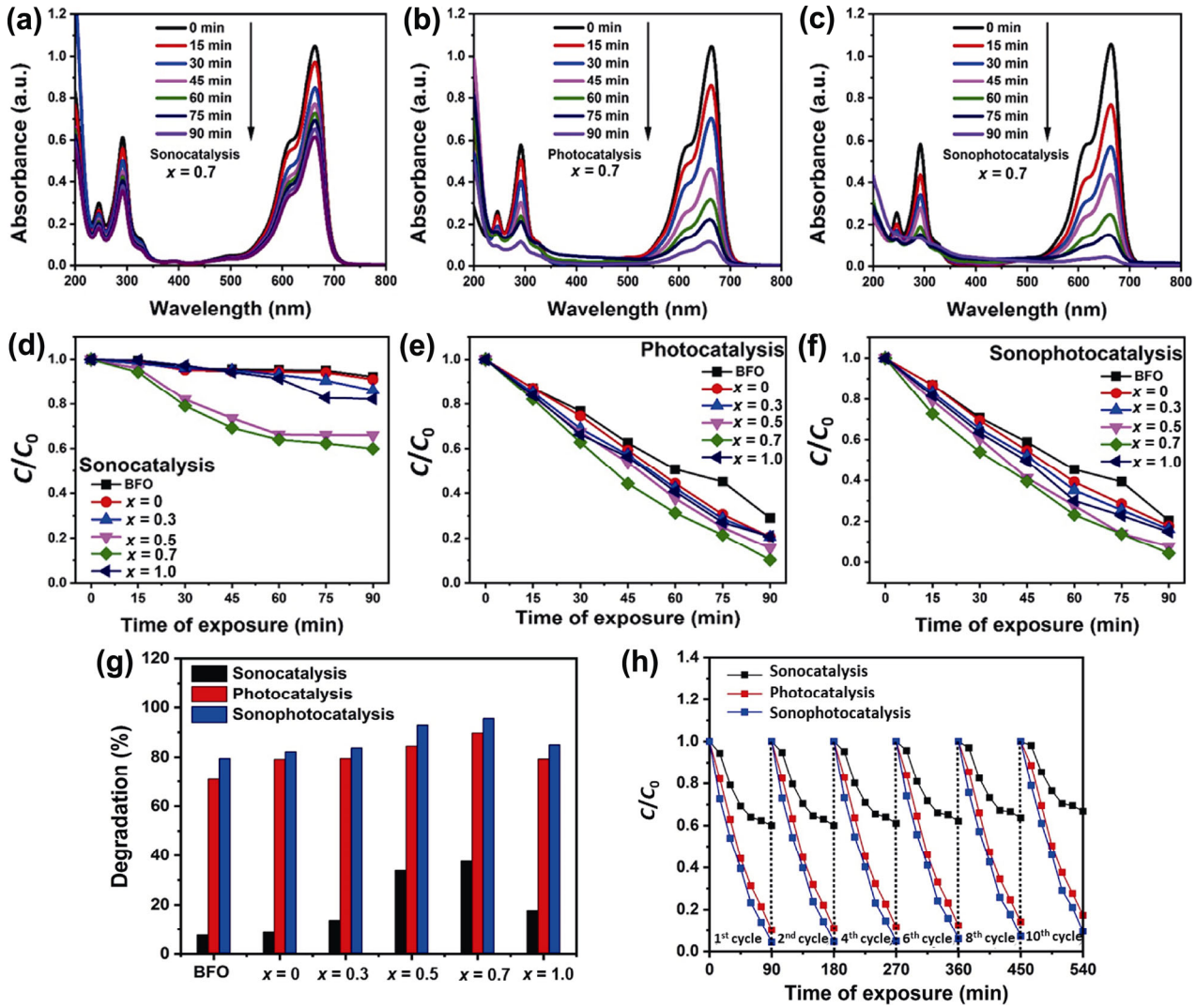

Fig. 6 Catalytic degradation performance of MB under different stimuli: (a–c) absorption spectra of MB solution after the degradation test using $Bi_{0.9}Gd_{0.07}La_{0.03}FeO_3$ nanotube with different exposure times under three different stimuli. (d–f) C/C_0 ratio of MB solution as a function of exposure time under three different stimuli. (g) Degradation efficiency under different stimuli for different Gd doping ratios and (h) degradation of MB under different stimuli for 10 cycles.

is achieved under dual stimuli. The $Bi_{0.9}Gd_{0.07}La_{0.03}FeO_3$ nanotube achieves 78% degradation of MB within 60 min and 95% degradation of MB within 90 min. The higher degradation efficiency obtained under dual stimuli than those under either solar or sonic excitation has also been observed with a range of catalysts, such as $Ag_2O/BaTiO_3$ [15] and BFO nanofibers [57]. A comprehensive comparison is listed in Table S2 in the ESM. The enhanced performance under simultaneous photoexcitation and sonication is attributed to the piezoelectric effect originating from the polarization of $Bi_{0.9}Gd_{0.07}La_{0.03}FeO_3$ during sonication. When the $Bi_{0.9}Gd_{0.07}La_{0.03}FeO_3$ nanotubes are harvesting photons, electrons transfer to the CB, leaving an equal number of holes in the VB. The piezoelectric potential forms in the $Bi_{0.9}Gd_{0.07}La_{0.03}FeO_3$ nanotubes when they are harvesting vibration energy, which facilitates the spatial separation of photo-generated electrons and holes at surface [11]. The enhanced separation of electrons and holes would further promote the redox reaction, therefore producing a synergy effect between the two catalytic processes.

Compared with the BFO nanotube, the sonocatalysis, photocatalysis, and sonophotocatalysis efficiencies of the $Bi_{0.9}Gd_{0.07}La_{0.03}FeO_3$ nanotube are always higher (Fig. 6(g)). This indicates that introducing OVs into the BFO enhances the catalytic performance. The sonocatalysis degradation of MB is increased by more than 4 times, while the photocatalysis degradation is increased by 26% for the $Bi_{0.9}Gd_{0.07}La_{0.03}FeO_3$ nanotubes.

For the BFO nanotube, a MB degradation of 80% for bi-catalysis is exactly the sum of the degradation by photocatalysis (71%) and sonocatalysis (9%). The MB degradation of bi-catalysis for the $Bi_{0.9}Gd_{0.07}La_{0.03}FeO_3$ (95%) is however lower than the sum of those for photocatalysis (89%) and sonocatalysis (37%). The lower synergistically catalytic activity than the sum of single catalysis has been also reported previously [10,18]. This might on the one hand be ascribed to the coupling effect between photocatalysis and sonocatalysis [62]. On the other hand, the carrier density is increased under dual stimuli, which increases the quenching probability of the charge carriers [63]. For the samples with a high concentration of OVs, the better catalytic performance under dual stimuli than that under single excitation indicates that the synergistic piezoelectric and photoelectric effect plays a predominant role, and the slight coupling effect only plays a minor role in the performance. The combination of the maximum charge separation and enhanced charge density overpower the high quenching probability to achieve the maximum catalytic degradation efficiency [11,64,65].

The reproducibility and stability of catalysts are crucial for practical application. After the MB degradation test, the catalyst was separated from the solution by centrifugation, washed thoroughly with water, and dried for the next degradation test. As shown in Fig. 6(h), obvious degradation of MB by $Bi_{0.9}Gd_{0.07}La_{0.03}FeO_3$ was observed within 10 cycles with each cycle operated for 90 min. The variation of catalytic degradation efficiency during cyclic process under different stimuli are more clearly shown in Fig. S7 in the ESM, from which gradual decrease of the catalytic efficiency can be seen. However, the catalyst still retained approximately 88% of its initial efficiency after 10 cycles, indicating good stability of the catalyst. The slight decrease of the efficiency might be due to the gradual poisoning and/or the change of the chemical structure/morphology of the catalyst.

4 Conclusions

Pristine BFO and doped $Bi_{0.9}(Gd_xLa_{1-x})_{0.1}FeO_3$ (x = 0, 0.3, 0.5, 0.7, and 1.0) nanotubes were synthesized by a simple electrospinning process. Increasing the doping content of Gd leads to an increase in the concentration of OVs in the $Bi_{0.9}(Gd_xLa_{1-x})_{0.1}FeO_3$ nanotubes, which reaches a maximum in $Bi_{0.9}Gd_{0.07}La_{0.03}FeO_3$. The generated OVs decrease the E_g, endow efficient charge separation, and enhance piezoelectric activity in the nanofibers, and thus significantly improve the sonocatalysis, photocatalysis, and sonophotocatalysis performance. Under simultaneous all-spectrum solar irradiation and ultrasonic excitation, the $Bi_{0.9}Gd_{0.07}La_{0.03}FeO_3$ nanotube shows the highest photocatalytic performance with 95% MB degradation in 90 min. Combining the effects of doping-induced OVs and mechanical strain leads to enhanced charge separation and efficient MB degradation. Such findings may promote the utilization of under-utilized mechanical energy such as noise and water motion as energy sources for environmental remediation.

Acknowledgements

This work was supported by the Shenzhen Government's Plan of Science and Technology (JCYJ20190808121407676), the Natural Science Foundation of Guangdong Province (2020A1515011127), and the Shenzhen University Initiative Research Program (2019005).

Electronic Supplementary Material

Supplementary material is available in the online version of this article at https://doi.org/10.1007/s40145-022-0590-6.

References

[1] Kou JH, Lu CH, Wang J, *et al*. Selectivity enhancement in heterogeneous photocatalytic transformations. *Chem Rev* 2017, **117**: 1445–1514.

[2] Yang WY, Chen Y, Gao S, *et al*. Post-illumination activity of Bi_2WO_6 in the dark from the photocatalytic "memory" effect. *J Adv Ceram* 2021, **10**: 355–367.

[3] Wu YY, Gao ZR, Li H, *et al*. Promoting carrier separation efficiently by macroscopic polarization charges and interfacial modulation for photocatalysis. *Chem Eng J* 2021, **410**: 128393.

[4] Ma LL, Yang C, Tian XK, *et al*. Enhanced usage of visible light by $BiSe_x$ for photocatalytic degradation of methylene blue in water via the tunable band gap and energy band position. *J Clean Prod* 2018, **171**: 538–547.

[5] Qiang TT, Chen L, Xia YJ, *et al*. Dual modified MoS_2/SnS_2 photocatalyst with Z-scheme heterojunction and vacancies defects to achieve a superior performance in Cr (VI) reduction and dyes degradation. *J Clean Prod* 2021, **291**: 125213.

[6] Sadeghzadeh-Attar A. Photocatalytic degradation evaluation of N–Fe codoped aligned TiO_2 nanorods based on the effect

of annealing temperature. *J Adv Ceram* 2020, **9**: 107–122.

[7] Shao YQ, Feng KK, Guo J, *et al*. Electronic structure and enhanced photoelectrocatalytic performance of $Ru_xZn_{1-x}O$/Ti electrodes. *J Adv Ceram* 2021, **10**: 1025–1041.

[8] Xi YM, Zhang Y, Cai XT, *et al*. PtCu thickness-modulated interfacial charge transfer and surface reactivity in stacked graphene/Pd@PtCu heterostructures for highly efficient visible-light reduction of CO_2 to CH_4. *Appl Catal B Environ* 2022, **305**: 121069.

[9] Zhong SX, Xi YM, Chen Q, *et al*. Bridge engineering in photocatalysis and photoelectrocatalysis. *Nanoscale* 2020, **12**: 5764–5791.

[10] Liu YL, Wu JM. Synergistically catalytic activities of $BiFeO_3/TiO_2$ core–shell nanocomposites for degradation of organic dye molecule through piezophototronic effect. *Nano Energy* 2019, **56**: 74–81.

[11] Ma JP, Ren J, Jia YM, *et al*. High efficiency bi-harvesting light/vibration energy using piezoelectric zinc oxide nanorods for dye decomposition. *Nano Energy* 2019, **62**: 376–383.

[12] Pan L, Sun SC, Chen Y, *et al*. Advances in piezo-phototronic effect enhanced photocatalysis and photoelectrocatalysis. *Adv Energy Mater* 2020, **10**: 2000214.

[13] Grinberg I, West DV, Torres M, *et al*. Perovskite oxides for visible-light-absorbing ferroelectric and photovoltaic materials. *Nature* 2013, **503**: 509–512.

[14] Xu SY, Guo LM, Sun QJ, *et al*. Piezotronic effect enhanced plasmonic photocatalysis by AuNPs/$BaTiO_3$ heterostructures. *Adv Funct Mater* 2019, **29**: 1808737.

[15] Li HD, Sang YH, Chang SJ, *et al*. Enhanced ferroelectric-nanocrystal-based hybrid photocatalysis by ultrasonic-wave-generated piezophototronic effect. *Nano Lett* 2015, **15**: 2372–2379.

[16] Li S, Zhao ZC, Yu DF, *et al*. Few-layer transition metal dichalcogenides (MoS_2, WS_2, and WSe_2) for water splitting and degradation of organic pollutants: Understanding the piezocatalytic effect. *Nano Energy* 2019, **66**: 104083.

[17] Xu J, Lu QL, Lin JF, *et al*. Enhanced ferro-/piezoelectric properties of tape-casting-derived Er^{3+}-doped $Ba_{0.85}Ca_{0.15}Ti_{0.9}Zr_{0.1}O_3$ optoelectronic thick films. *J Adv Ceram* 2020, **9**: 693–702.

[18] Yu DF, Liu ZH, Zhang JM, *et al*. Enhanced catalytic performance by multi-field coupling in $KNbO_3$ nanostructures: Piezo-photocatalytic and ferro-photoelectrochemical effects. *Nano Energy* 2019, **58**: 695–705.

[19] Fan KH, Yu C, Cheng ST, *et al*. Metallic Bi self-deposited BiOCl promoted piezocatalytic removal of carbamazepine. *Surf Interfaces* 2021, **26**: 101335.

[20] Li H, Li J, Ai ZH, *et al*. Oxygen vacancy-mediated photocatalysis of BiOCl: Reactivity, selectivity, and perspectives. *Angew Chem Int Ed* 2018, **57**: 122–138.

[21] Chen XB, Liu L, Yu PY, *et al*. Increasing solar absorption for photocatalysis with black hydrogenated titanium dioxide nanocrystals. *Science* 2011, **331**: 746–750.

[22] Corby S, Francàs L, Kafizas A, *et al*. Determining the role of oxygen vacancies in the photoelectrocatalytic performance of WO_3 for water oxidation. *Chem Sci* 2020, **11**: 2907–2914.

[23] Guo HL, Zhu Q, Wu XL, *et al*. Oxygen deficient ZnO_{1-x} nanosheets with high visible light photocatalytic activity. *Nanoscale* 2015, **7**: 7216–7223.

[24] Wang YC, Wu JM. Effect of controlled oxygen vacancy on H_2-production through the piezocatalysis and piezophototronics of ferroelectric *R*3*C* $ZnSnO_3$ nanowires. *Adv Funct Mater* 2020, **30**: 1907619.

[25] Ou G, Li DK, Pan W, *et al*. Arc-melting to narrow the bandgap of oxide semiconductors. *Adv Mater* 2015, **27**: 2589–2594.

[26] You HL, Wu Z, Zhang LH, *et al*. Harvesting the vibration energy of $BiFeO_3$ nanosheets for hydrogen evolution. *Angew Chem Int Ed* 2019, **58**: 11779–11784.

[27] Catalan G, Scott JF. Physics and applications of bismuth ferrite. *Adv Mater* 2009, **21**: 2463–2485.

[28] Xia L, Tybell T, Selbach SM. Bi vacancy formation in $BiFeO_3$ epitaxial thin films under compressive (001)-strain from first principles. *J Mater Chem C* 2019, **7**: 4870–4878.

[29] Noguchi Y, Matsuo H, Kitanaka Y, *et al*. Ferroelectrics with a controlled oxygen-vacancy distribution by design. *Sci Rep* 2019, **9**: 4225.

[30] Yu YG, Chen G, Zhou YS, *et al*. Recent advances in rare-earth elements modification of inorganic semiconductor-based photocatalysts for efficient solar energy conversion: A review. *J Rare Earths* 2015, **33**: 453–462.

[31] Purusottam Reddy B, Park SH. Improved photocatalytic activity of $BiFeO_3$ nanoparticles upon Gd doping. In: Proceedings of the 2nd International Conference on Inventive Research in Material Science and Technology, Coimbatore, India, 2019: 020001.

[32] Lan SY, Yu C, Sun F, *et al*. Tuning piezoelectric driven photocatalysis by La-doped magnetic $BiFeO_3$-based multiferroics for water purification. *Nano Energy* 2022, **93**: 106792.

[33] Yang GD, Chen Q, Wang WJ, *et al*. Cocatalyst engineering in piezocatalysis: A promising strategy for boosting hydrogen evolution. *ACS Appl Mater Interfaces* 2021, **13**: 15305–15314.

[34] Reddy BP, Sekhar MC, Prakash BP, *et al*. Photocatalytic, magnetic, and electrochemical properties of La doped $BiFeO_3$ nanoparticles. *Ceram Int* 2018, **44**: 19512–19521.

[35] Gao F, Chen XY, Yin KB, *et al*. Visible-light photocatalytic properties of weak magnetic $BiFeO_3$ nanoparticles. *Adv Mater* 2007, **19**: 2889–2892.

[36] Suresh P, Babu PD, Srinath S. Role of (La,Gd) co-doping on the enhanced dielectric and magnetic properties of $BiFeO_3$ ceramics. *Ceram Int* 2016, **42**: 4176–4184.

[37] Fan HJ, Gösele U, Zacharias M. Formation of nanotubes and hollow nanoparticles based on Kirkendall and diffusion processes: A review. *Small* 2007, **3**: 1660–1671.

[38] Yin YD, Rioux RM, Erdonmez CK, *et al*. Formation of hollow nanocrystals through the nanoscale Kirkendall effect. *Science* 2004, **304**: 711–714.

[39] Ji DX, Fan L, Tao L, *et al*. The Kirkendall effect for engineering oxygen vacancy of hollow Co_3O_4 nanoparticles toward high-performance portable zinc–air batteries. *Angew Chem Int Ed* 2019, **58**: 13840–13844.

[40] Irfan S, Rizwan S, Shen Y, *et al*. The gadolinium (Gd^{3+}) and tin (Sn^{4+}) co-doped $BiFeO_3$ nanoparticles as new solar light active photocatalyst. *Sci Rep* 2017, **7**: 42493.

[41] Zhang N, Chen D, Niu F, *et al*. Enhanced visible light photocatalytic activity of Gd-doped $BiFeO_3$ nanoparticles and mechanism insight. *Sci Rep* 2016, **6**: 26467.

[42] Kumar M, Arora M, Chauhan S, *et al*. Raman spectroscopy probed spin–two phonon coupling and improved magnetic and optical properties in Dy and Zr substituted $BiFeO_3$ nanoparticles. *J Alloys Compd* 2017, **692**: 236–242.

[43] Yang Y, Sun JY, Zhu K, *et al*. Raman study of $BiFeO_3$ with different excitation wavelengths. *Phys B Condens Matter* 2009, **404**: 171–174.

[44] Das S, Nayak GC, Sahu SK, *et al*. Microwave absorption properties of double-layer composites using CoZn/NiZn/MnZn-ferrite and titanium dioxide. *J Magn Magn Mater* 2015, **377**: 111–116.

[45] Yang TT, Wei J, Guo YX, *et al*. Manipulation of oxygen vacancy for high photovoltaic output in bismuth ferrite films. *ACS Appl Mater Interfaces* 2019, **11**: 23372–23381.

[46] Qiao L, Bi XF. Direct observation of oxygen vacancy and its effect on the microstructure, electronic and transport properties of sputtered $LaNiO_{3-\delta}$ films on Si substrates. *Thin Solid Films* 2010, **519**: 943–946.

[47] Tan HQ, Zhao Z, Zhu WB, *et al*. Oxygen vacancy enhanced photocatalytic activity of pervoskite $SrTiO_3$. *ACS Appl Mater Interfaces* 2014, **6**: 19184–19190.

[48] Miriyala N, Prashanthi K, Thundat T. Oxygen vacancy dominant strong visible photoluminescence from $BiFeO_3$ nanotubes. *Phys Status Solidi RRL Rapid Res Lett* 2013, **7**: 668–671.

[49] Yang B, Bian JH, Wang L, *et al*. Enhanced photocatalytic activity of perovskite $NaNbO_3$ by oxygen vacancy engineering. *Phys Chem Chem Phys* 2019, **21**: 11697–11704.

[50] Lan SY, Yu C, Wu EY, *et al*. Self-powered water flow-triggered piezocatalytic generation of reactive oxygen species for water purification in simulated water drainage. *ACS EST Eng* 2022, **2**: 101–109.

[51] Liao ZM, Liu KJ, Zhang JM, *et al*. Effect of surface states on electron transport in individual ZnO nanowires. *Phys Lett A* 2007, **367**: 207–210.

[52] Liao ZM, Zhang HZ, Zhou YB, *et al*. Surface effects on photoluminescence of single ZnO nanowires. *Phys Lett A* 2008, **372**: 4505–4509.

[53] Wang D, Seo HW, Tin CC, *et al*. Effects of postgrowth annealing treatment on the photoluminescence of zinc oxide nanorods. *J Appl Phys* 2006, **99**: 113509.

[54] Jenkins K, Kelly S, Nguyen V, *et al*. Piezoelectric diphenylalanine peptide for greatly improved flexible nanogenerators. *Nano Energy* 2018, **51**: 317–323.

[55] Tao K, Xue B, Li Q, *et al*. Stable and optoelectronic dipeptide assemblies for power harvesting. *Mater Today* 2019, **30**: 10–16.

[56] Xie SH, Gannepalli A, Chen QN, *et al*. High resolution quantitative piezoresponse force microscopy of $BiFeO_3$ nanofibers with dramatically enhanced sensitivity. *Nanoscale* 2012, **4**: 408–413.

[57] Mushtaq F, Chen XZ, Hoop M, *et al*. Piezoelectrically enhanced photocatalysis with $BiFeO_3$ nanostructures for efficient water remediation. *iScience* 2018, **4**: 236–246.

[58] Fei LF, Hu YM, Li X, *et al*. Electrospun bismuth ferrite nanofibers for potential applications in ferroelectric photovoltaic devices. *ACS Appl Mater Interfaces* 2015, **7**: 3665–3670.

[59] Mani AD, Soibam I. Dielectric, magnetic and optical properties of $(Bi,Gd)FeO_3$–$Ni_{0.8}Zn_{0.2}Fe_2O_4$ nanocomposites. *Ceram Int* 2018, **44**: 2419–2425.

[60] Flint EB, Suslick KS. The temperature of cavitation. *Science* 1991, **253**: 1397–1399.

[61] Talukdar S, Dutta RK. A mechanistic approach for superoxide radicals and singlet oxygen mediated enhanced photocatalytic dye degradation by selenium doped ZnS nanoparticles. *RSC Adv* 2016, **6**: 928–936.

[62] Zhao K, Ouyang BS, Yang Y. Enhancing photocurrent of radially polarized ferroelectric $BaTiO_3$ materials by ferro-pyro-phototronic effect. *iScience* 2018, **3**: 208–216.

[63] Wang SS, Wu Z, Chen J, *et al*. Lead-free sodium niobate nanowires with strong piezo-catalysis for dye wastewater degradation. *Ceram Int* 2019, **45**: 11703–11708.

[64] Park BW, Zhang XL, Johansson EMJ, *et al*. Analysis of crystalline phases and integration modelling of charge quenching yields in hybrid lead halide perovskite solar cell materials. *Nano Energy* 2017, **40**: 596–606.

[65] Zhu SS, Wang DW. Photocatalysis: Basic principles, diverse forms of implementations and emerging scientific opportunities. *Adv Energy Mater* 2017, **7**: 1700841.